Inorganic Chemistry

pubs.acs.org/IC Article

Influence of the Cubic Sublattice on Magnetic Coupling between the Tetrahedral Sites of Garnet

JoAnna Milam-Guerrero, Michelle Zheng, Nicole R. Spence, Mario Falsaperna, Stuart Calder, Saul Lapidus, Paul J. Saines, and Brent C. Melot*

Cite This: *Inorg. Chem.* 2021, 60, 8500–8506 Read Online

ACCESS | Metrics & More | Article Recommendations | Supporting Information

ABSTRACT: We present a study on the nuclear and magnetic structures of two iron-based garnets with magnetic cations isolated on tetrahedral sites. $Ca_2YZr_2Fe_3O_{12}$ and $Ca_2LaZr_2Fe_3O_{12}$ offer an interesting comparison for examining the effect of increasing cation size within the diamagnetic backbone of the garnet crystal structure, and how such changes affect the magnetic order. Despite both systems exhibiting well-pronounced magnetic transitions at low temperatures, we also find evidence for diffuse magnetic scattering due to a competition between the nearest-neighbor, next nearest-neighbor, and so on, within the tetrahedral sites. This competition results in a complex noncollinear magnetic structure on the tetrahedral sublattice creating a mixture of ferro- and antiferromagnetic interactions above the long-range ordering temperature near 20 K and suggests that the cubic site of the garnet plays a significant role in mediating the superexchange interactions between tetrahedral cations.

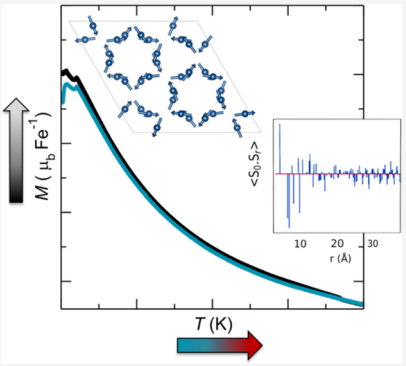

INTRODUCTION

$Y_3Fe_5O_{12}$ garnet (YIG) has been extensively studied due to its widespread use as a magnetic material with many commercial applications.[1−8] Yet, many questions remain about the fundamental magnetic interactions in garnets, which is due, in large part, to the multiple sublattices and vast compositional diversity available. Garnets adopt the general formula $R_3B_2A_3O_{12}$ with three uniquely coordinated environments that can accommodate a wide swath of the periodic table, making them an ideal test system for exploring structure−property relationships (see Figure 1).

To better understand the magnetic coupling within each sublattice, individual sites must be isolated from one another by forcing magnetic cations to occupy a single site through a judicious selection of diamagnetic components in the material.[9] A great deal of work has been done in this regard to study the magnetism of octahedral and cubic sites in materials like $Gd_3Ga_5O_{12}$,[6−8] $Mn_3Al_2Ge_3O_{12}$,[10,11] $Mn_3Al_2Si_3O_{12}$,[11,12] $CaY_2Co_2Ge_3O_{12}$,[13] and $Ca_3Cr_2Ge_3O_{12}$.[14] Yet, keeping cations with open valence shells on the tetrahedral site is far more challenging due to the lack of magnetic cations with a strong preference for a tetrahedral coordination environment. Instead, the simplest way to study the tetrahedral sublattice is to select cations that localize strongly to cubic and octahedral sites, which then indirectly force more site-promiscuous cations to stay in place. To date, only a few studies have examined the magnetism of the tetrahedral sublattice in materials like $Na_3Te_2Fe_3O_{12}$, $Ca_3SnSbFe_3O_{12}$, $NaCa_2Sb_2Fe_3O_{12}$, and $Ca_3ZrSbFe_3O_{12}$.[15]

As early as 1964, Geller et al.[16] had begun to explore the magnetism of the tetrahedral sublattice and, while they were unable to prepare phase-pure samples, they hypothesized that compositions like $Ca_2YZr_2Fe_3O_{12}$ should be fully ordered with Zr on the octahedral site and Fe in the tetrahedra, but would only exhibit short-range antiferromagnetic order.[16] Dodokin et al.[15] later used Mössbauer spectroscopy to study the orientation of the moments on the tetrahedra and found that spins no longer ordered along [111] when iron is removed from octahedral sites. At the time, this was attributed to the extremely weak coupling seen between the tetrahedra, which is roughly an order of magnitude less than that of the octahedra.

In this report, we sought to more carefully examine the ground-state magnetic order of the tetrahedral sublattice in $Ca_2YZr_2Fe_3O_{12}$ and $Ca_2LaZr_2Fe_3O_{12}$, which only differ through a minor change in the size of diamagnetic ions on the cubic site. Interestingly, we find that both materials exhibit clear signs of long-range magnetic order, but also show more subtle evidence at higher temperatures for short-range correlations between the spins that manifest as a result of through-cubic polyhedra superexchange pathways. To better understand this short-range magnetic order, we employ Reverse Monte-Carlo (RMC) methods to model the

Received: January 12, 2021
Published: June 2, 2021

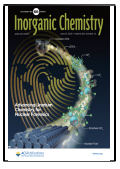

https://doi.org/10.1021/acs.inorgchem.1c00113
Inorg. Chem. 2021, 60, 8500–8506

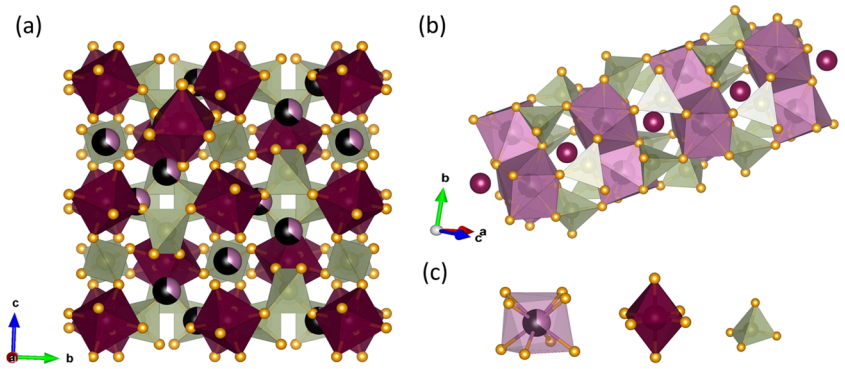

Figure 1. (a) Ideal cubic garnet unit cell along one equivalent axis. (b) Looking at a single rod with the octahedral center surrounded by alternating cubic and tetrahedral sites. (c) From left to right, the cubic site is depicted in black and pink indicating a mixed cation occupation (R, eight-coordinated), the octahedral site as maroon (B, six-coordinated), and the tetrahedral site as light green (A, four-coordinated).

contribution of magnetism to the magnetic diffuse scattering data, which supports a noncollinear antiferromagnetic arrangement of the moments in the ordered structure arising from magnetic frustration, thus highlighting the importance of the cubic sublattice.

EXPERIMENTAL SECTION

Synthesis. Polycrystalline samples were synthesized by grinding stoichiometric ratios of $CaCO_3$, Y_2O_3, La_2O_3, ZrO_2, and Fe_2O_3 and pressing into pellets before sintering in air in multiple heating treatments. All pellets were heated on a layer of sacrificial powder to isolate them from the zirconia crucible. Samples were first heated to 900 °C for 6 h in air to decompose carbon-containing starting materials. Samples were subsequently heated at 1250 °C for 24 h in air until phase pure.

Structure Determination. Sample purity and potential site mixing were evaluated using both X-ray and neutron diffraction. Powder XRD was performed at room temperature using 11-BM at Argonne National Laboratory at λ = 0.457861 and 0.412797 Å for $Ca_2YZr_2Fe_3O_{12}$ and $Ca_2LaZr_2Fe_3O_{12}$, respectively, while neutron diffraction data was collected at the HB-2A high-resolution neutron powder diffractometer at the High Flux Isotope Reactor at Oak Ridge National Laboratory.

Physical Property Measurements. Temperature- and field-dependent DC magnetic susceptibility, AC magnetic susceptibility, and heat capacity were measured on a Quantum Design 14T Dynacool Physical Property Measurement System. All magnetic measurements were performed on bulk powder samples held in place using eicosane wax. Heat capacity measurements were measured on powdered samples mixed with equal parts silver to increase the thermal coupling to the sample stage. The silver and epoxy contributions were measured separately and subtracted out.[17]

RMC-SPINVERT. Since the diffuse magnetic neutron scattering was strongest in the 18 K data of the $Ca_2YZr_2Fe_3O_{12}$ phase, this was isolated by removal of the nuclear scattering through subtraction of the 100 K data set. The data were then placed on an absolute intensity scale (barn sr^{-1} Fe^{-1}) by normalization to the calculated nuclear Bragg profile from the 100 K data set. This diffuse magnetic scattering was subsequently fitted using the RMC program—SPINVERT,[18] using a supercell of 6 × 6 × 6 units of the cubic crystal structure with a total volume of 442 284 Å^3. Spins in these refinements were refined as three-dimensional vectors, as expected for tetrahedral d^5 Fe^{3+} magnetic cations, with magnetic moments fixed to 5.92 μ_B and standard analytical magnetic form factors. The value of 5.92 μ_B was chosen to reflect the expected magnetic moment that an octahedrally coordinated Fe^{3+} will experience in a high-spin coordination environment.

RESULTS AND DISCUSSION

Both $Ca_2YZr_2Fe_3O_{12}$ and $Ca_2LaZr_2Fe_3O_{12}$ exhibit signatures of antiferromagnetic order in the DC magnetic susceptibility starting near 18 and 21 K, respectively, but, more interestingly, these sharp peaks were followed by more broadened features starting around 10 K ($Ca_2YZr_2Fe_3O_{12}$) and 7 K ($Ca_2LaZr_2Fe_3O_{12}$), as seen in the insets of Figure 2. When

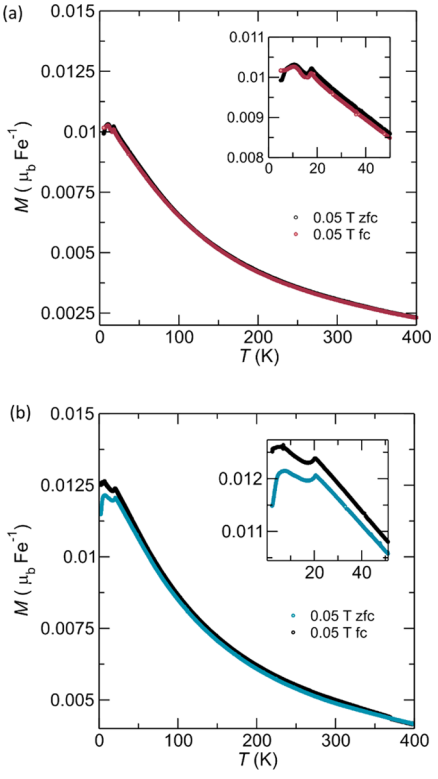

Figure 2. Temperature-dependent DC magnetic susceptibility under 500 Oe from 2 to 400 K. (a) $Ca_2YZr_2Fe_3O_{12}$ orders at 18 K and (b) $Ca_2LaZr_2Fe_3O_{12}$ orders at 21 K.

completely removing magnetic cations from the octahedral site, it comes as no surprise that the ordering temperature would drop from the 570 K transition seen in YIG to the low temperatures found for $Ca_2MZr_2Fe_3O_{12}$, but it is somewhat unexpected that the tetrahedral sublattice would order as high as 20 K given the lack of short superexchange pathways. Yet, extensive work on ferrimagnets like YIG has clearly shown that

https://doi.org/10.1021/acs.inorgchem.1c00113
Inorg. Chem. 2021, 60, 8500−8506

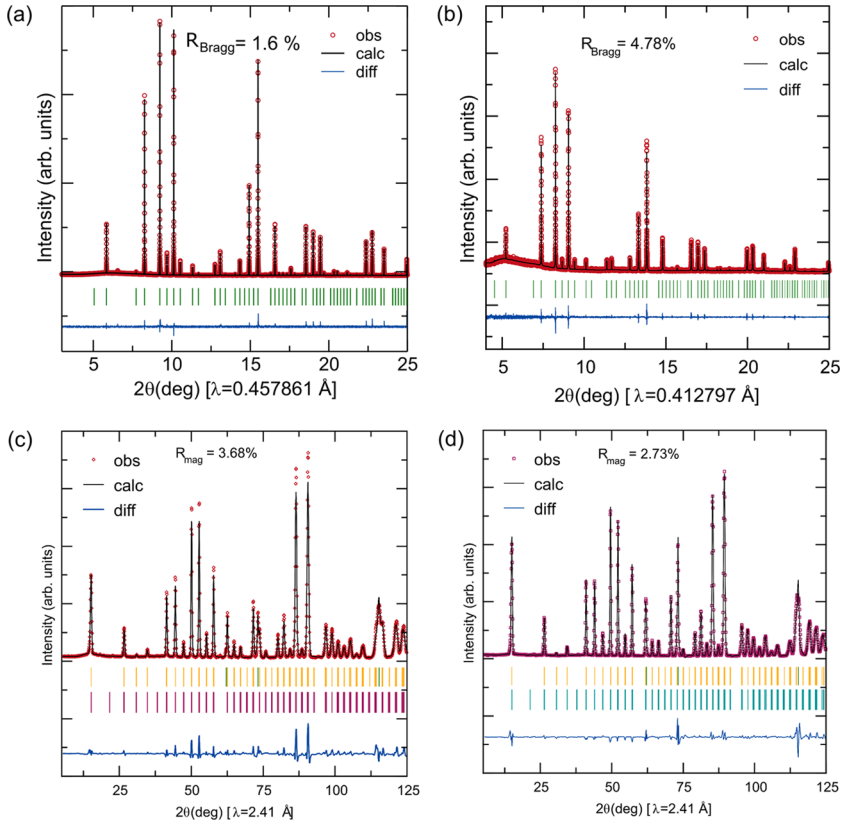

Figure 3. Results of structural refinement against X-ray and neutron data of $Ca_2YZr_2Fe_3O_{12}$ and $Ca_2LaZr_2Fe_3O_{12}$ in the left and right column, respectively. (a, b) Rietveld fits of X-ray powder diffraction powders from 11-BM at 295 K. The red circles, black line, and blue line represent the observed pattern, fitting line, and difference line, respectively. (c, d) Refined fits from the corresponding neutron powder diffraction data at 1.5 K with the vanadium sample can (dark green) be used in the experiment. Nuclear reflections are highlighted in yellow on the first row, while the magnetic reflections are on the second row.

the antiferromagnetic tetrahedra−tetrahedra (A−A) coupling is stronger than antiferromagnetic octahedra−octahedra (B−B) interactions.[16] More unexpected is the presence of two magnetic ordering transitions since this type of order is more common for materials containing multiple magnetic sublattices as in $Mn_3Cr_2Ge_3O_{12}$.[1919] So given that Fe^{3+} has very little preference to sit on any one of the sites within the garnet structure, care was taken to rule out any cation mixing between the sites or the presence of minute paramagnetic impurities.

As such, X-ray and neutron powder diffraction were collected at Argonne and Oak Ridge National Laboratory, respectively, to fully characterize the nuclear and magnetic structure. Both data sets were carefully refined and showed no evidence for any site mixing of Fe onto the octahedral or cubic site as demonstrated in Figure 3, with the relevant parameters from the refinement given in Tables S2 and S3. This strongly suggests that both features in the magnetic susceptibility are associated solely with the tetrahedral site. Fitting the high-temperature region (150−300 K) of the susceptibility to the Curie−Weiss equation and including a temperature-independent paramagnetic contribution, $\chi = C/(T - \Theta_{CW}) + \chi_0$, yields a Θ_{CW} of −85 K (−82 K) and an effective paramagnetic moment of 6.1 (6.2) μ_B per Fe and $\chi_0 = 9.4 \times 10^{-4}$ (5.5×10^{-3}) emu mol^{-1} Oe^{-1} for the Y and La analogue, respectively. This moment is in close agreement with the expected value for Fe^{3+} 5.92 μ_B in a high-spin tetrahedral coordination environment (d^5, $S = 5/2$, $L = 0$).[20] The negative sign of Θ_{CW} indicates that antiferromagnetic exchange is dominant between the spins and that there is a modest suppression of the ordering temperature due to geometrical competition between the exchange interactions.

Neutron powder diffraction was performed at several temperatures around magnetic transitions to monitor the onset of magnetic order. As the temperature is decreased, magnetic reflections gradually appear, as seen in Figure 4a,b for $Ca_2YZr_2Fe_3O_{12}$ and $Ca_2LaZr_2Fe_3O_{12}$, respectively. The higher angle magnetic peaks appear sharply below the respective ordering temperatures as is expected when new scattering planes are created as the thermal energy is no longer sufficient to disrupt the cooperative ordering of the spins and the spins form an ordered structure over a relatively small temperature range. This contrasts with the peak at 15°, for both samples, where a diffuse peak slowly begins to evolve well above the peak in the susceptibility and gradually shifts to lower θ until the sharp appearance of the magnetically ordered Bragg peak. This diffuse peak continues to grow with decreasing temperature as well as shifting to slightly lower θ as illustrated in Figures 4 and S5.

At all temperatures within the paramagnetic state, the Bragg reflections in the neutron data are fit well using solely the cubic $Ia\bar{3}d$ nuclear structure of the garnet. Below the ordering temperature, additional peaks appear at 15, 47, 67, and 84° with a magnetic contribution to several of the nuclear peaks at 26, 35, and 41°. Representational analysis was used to fit the neutron data at 1.5 K with the following associated magnetic reflections at: 15, 26, 35, 41, 47, 67, and 84°. All of the observed magnetic reflections were indexed using the propagation vector $\mathbf{k} = 0$, but within the space group $R\bar{3}c$

https://doi.org/10.1021/acs.inorgchem.1c00113
Inorg. Chem. 2021, 60, 8500−8506

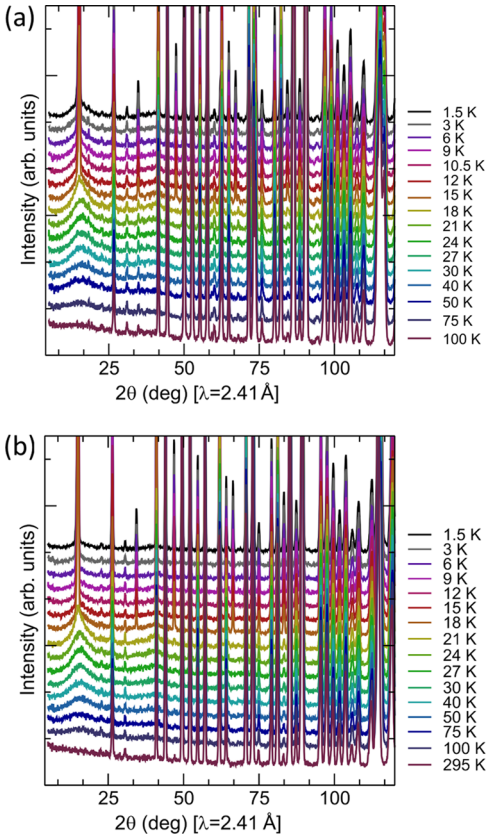

Figure 4. Temperature-dependent neutron data for each composition where symmetry-allowed magnetic peaks appear at (a) 18 K for $Ca_2YZr_2Fe_3O_{12}$ and (b) 21 K for $Ca_2LaZr_2Fe_3O_{12}$. Both compositions have a dynamic diffuse scattering peak at the (101) reflection (15°) before the system order.

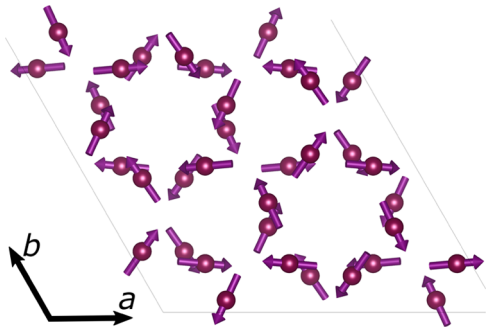

Figure 5. Resulting magnetic structure of $Ca_2YZr_2Fe_3O_{12}$ at 1.5 K. While both compositions are refined using the same representation, $Ca_2LaZr_2Fe_3O_{12}$ is presented in Figure S6.

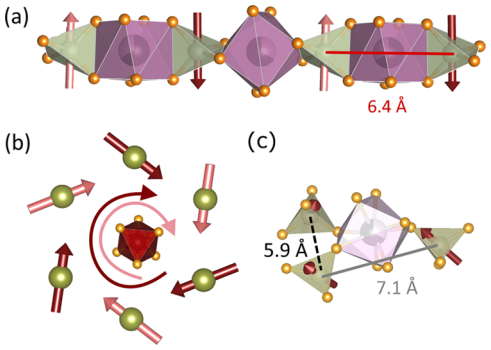

Figure 6. To understand the source of competing exchange interactions, intrarod interactions are plotted where (a) the two sets of tetrahedra from different rods are antiferromagnetic to each other. (b) Looking along the rod, the sets of tetrahedra on opposite faces of the dodecahedra are ferromagnetic to each other. (c) Tetrahedra are edge-sharing with dodecahedra between different rods and corner-sharing with dodecahedra along the same rod. Iron to iron distances are shown.

(#167), which corresponds to a $\sqrt{2} \times \sqrt{2} \times 2$ supercell of the cubic structure.[21] The space group symmetry was lowered based on previous reports that the magnetic structure of iron-based garnets can be more accurately modeled using trigonal space groups.[9,22,23] For example, it has been observed that the magnetic structure of YIG cannot be described well using cubic symmetry, but instead $R\bar{3}$ achieves better agreement with bulk magnetometry. $R\bar{3}c$ was chosen by examining possible subgroup relationships to $R\bar{3}$ using Bilbao Crystallographic Server.[24,25]

Symmetry analysis of the magnetic structure was performed using SARAh,[26] which returned five one-dimensional and one two-dimensional representations within the Little Group G_k. Both compositions were fit using the fourth representation, Γ_4, as seen fit in Figure 3 and illustrated in Figures 5 and 6. This representation consists of the basis vectors listed in Table S1 and produces a noncollinear arrangement of the spins that wraps around the rods as seen in Figure 5. Within $R\bar{3}c$, the rods are oriented along the *c*-axis with the majority of the magnetic moment laying within the *ab*-plane rather than simply aligning along a common easy axis. The magnetic moment at 1.5 K refined to a value of 3.28 and 3.97 μ_B for $Ca_2YZr_2Fe_3O_{12}$ and $Ca_2LaZr_2Fe_3O_{12}$, respectively, and is in agreement with the isothermal $M-H$ measurements, which exhibit a linear response (Figure S3) and fail to saturate by 14 T at 2 K and only reach a maximum value of 2.59 and 2.79 μ_B for $Ca_2YZr_2Fe_3O_{12}$ and $Ca_2LaZr_2Fe_3O_{12}$, respectively.

Below the ordering temperature, the moments are consistently larger in the La-based composition, which we attribute to the higher covalent character of La versus that of Y. In an eight-coordinate environment, lanthanum(III) and yttrium(III) have ionic radii of 1.160 and 1.019 Å, respectively. The smaller radius of yttrium is sufficient, even at only one-third occupancy of the cubic site, to cause the unit cell to decrease from 12.81870(1) to 12.529387(2) Å (at 295 K from synchrotron X-ray powder diffraction), which increases Zr−O bond lengths in the octahedra from 2.059(1) to 2.068(4) Å. Similarly, Fe−O bonds in the tetrahedra increase from 1.869(1) to 1.898(4) Å, yet this is offset by a contraction of the cubic metal−oxygen bond lengths from 2.455(4) to 2.381(1) Å. Thus, $Ca_2YZr_2Fe_3O_{12}$ contains longer tetrahedral and octahedral metal−oxygen bonds indicating higher covalency for the lanthanum cation over that of the yttrium cation.

The octahedral sites are commonly believed to have the largest influence on the magnetic coupling within the garnet structure; however, in this instance, the cubic site appears to play a more considerable role. This is best seen by examining the coupling between the tetrahedral sites, as illustrated in Figure 6a, which shows that the seemingly complex noncollinear magnetic structure can be viewed more simply as an antiferromagnetic coupling across the shared edges of cubic and tetrahedral sites. While this is slightly surprising given that these neighboring spins correspond to the second-nearest-

https://doi.org/10.1021/acs.inorgchem.1c00113
Inorg. Chem. 2021, 60, 8500−8506

neighboring pairs of spin, there are many more degenerate pathways through which the moments can interact through the shared edges of the polyhedra compared to the corner-sharing nature of the nearest neighbors. Figure 6b,c further shows that two ferromagnetic sublattices of spins are present (illustrated as pink and dark red) and couple antiferromagnetically to each other to form a spiral revolving around the octahedral chains. So, while the unit cell of $Ca_2LaZr_2Fe_3O_{12}$ may be larger, the shorter bond lengths in the tetrahedra produce stronger superexchange pathways, which makes the ordering temperature slightly higher than that of $Ca_2YZr_2Fe_3O_{12}$ due to the improved covalent character from the enhanced orbital overlap.

To further understand the magnetic order in these materials, specific heat measurements were performed from 2 to 200 K. As shown in Figure S2, both specific heat measurements exhibit a sharp asymmetric λ-like anomaly at the respective magnetic ordering temperatures, which is a common indication of a second-order phase transition and suggests a long-range collective magnetic transition. Yet, the absence of a similar feature near the temperatures corresponding to the broad feature in the magnetic susceptibility suggests a less collective short-range change in the ordering of the spins. AC magnetic susceptibility measurements were, therefore, used to explore the possibility of short-range ordering or glassy features at various AC frequencies, shown in Figure S4. Two maxima occur at the same temperatures as those in the DC susceptibility and show no frequency dependence, which seems to rule out the presence of glassy domains in the material. We, therefore, tentatively attribute the broad feature in the susceptibility, the diffuse scattering in the neutron powder diffraction, and the deviation between the zero-field-cooled and field-cooled data to a small and uncompensated moment associated with short-range magnetic correlations.

To better understand the nature of these short-range magnetic correlations, the diffuse magnetic scattering data for $Ca_2YZr_2Fe_3O_{12}$ at 18 K, where the diffuse scattering was strongest, was fitted using SPINVERT with consistent results obtained across a large number of refinements with a typical fit of χ^2 of 13.5 as seen in Figure 7. Stereographic projections of the refined spin orientations, both from individual refinements and averaged out over all refinements, were examined and did not show any indication of preferential alignment within the unit cell. To confirm this, refinements were carried out in which the spin was, artificially, constrained to be oriented along the [100], [110], and [111] directions. No significant deterioration in the fits was observed, which suggests that the data obtained is insensitive to the absolute orientation of the spins with respect to crystallographic axes.

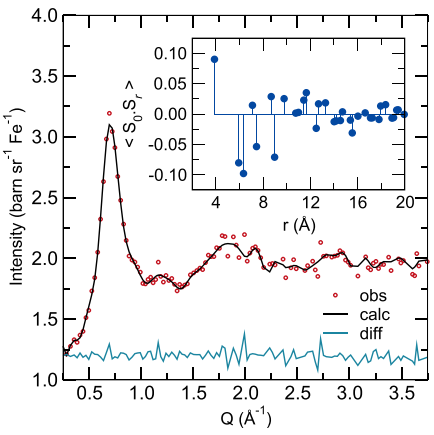

Figure 7. Results from the RMC fitting of the diffuse scattering, using Heisenberg-like spins, of $Ca_2YZr_2Fe_3O_{12}$ measured at 18 K. Data is shown in red, fit in black, and the difference in blue. (inset) Spin correlation $\langle S_0 \cdot S_r \rangle$ versus r from RMC fits to the diffuse magnetic scattering of $Ca_2YZr_2Fe_3O_{12}$, averaged over 300 refinements. Errors in the values are smaller than the circular markers.

If, as is typically the case in metal oxides, the separation between Fe atoms is sufficient that magnetic interactions must be facilitated by superexchange examination of the crystal structure reveals that this must occur via five atom superexchange bridges. For the nearest neighbors and closest three Fe−Fe neighbors with antiferromagnetic interactions, coupling is possible through a combination of Fe−O−Zr−O−Fe and Fe−O−Ca/Y−O−Fe pathways, although the latter should presumably be more significant due to the greater radial extension of Zr 4d orbitals. It should also be noted at this point that the Fe cations separated by ≈7.4 Å lack any direct links through the zirconium octahedra, which may explain its weaker antiferromagnetic correlations. The complex nature of these superexchange pathways makes it difficult to understand why the nearest neighbors and other significant correlations have opposite signs.

Comparison of the correlations obtained from the paramagnetic phase and the ordered antiferromagnetic structure provides a likely explanation for the noncollinear spins in the ordered structure and the role this plays in reducing the magnetic frustration in this structure. Comparing the distances, for which there are likely superexchange pathways in terms of increasing distance, we will start with the nearest neighbors. Here, examination of the Fe sites in the ordered structure shows that the spins for all sites have angles of less than 90° with at least three of the neighboring spins and the average of all of these angles with their four neighbors less than 90°. In contrast, for the spins of the Fe atoms separated by ≈5.9 Å from each other in the ordered structure, neighboring spins all have greater than a 90° angle from each other but are typically far from the 180° expected of purely antiferromagnetic correlations. For the Fe−Fe atoms separated by ≈6.4 Å, where the refined antiferromagnetic correlations are the strongest, there are only very small canting angles that prevent spins from being antiferromagnetically coupled to each other. Finally, for Fe cations separated by ≈7.4 Å, which have the weakest of the significant antiferromagnetic correlations in the paramagnetic phase, the spins on each Fe site have an angle of less than 90° with at least three of their four neighbors and the average of all of these angles with their four neighbors are less than 90°. Thus, it appears that for the three Fe−Fe distances for which significant correlations are observed in the paramagnetic phase it appears that, on average, the ordered phase satisfies the sign of the correlation expected from the paramagnetic phase. For Fe cations for which significant magnetic correlations can be identified as arising from a superexchange pathway, this pattern breaks down only for Fe−Fe distances of ≈7.4 Å, but this is consistent with their weaker antiferromagnetic correlations in the paramagnetic phase, likely a result of the lack of Fe−O−Zr−O−Fe superexchange pathways. This suggests that the highly canted structure plays a key role in satisfying the magnetic correlations expected from the paramagnetic phase.

https://doi.org/10.1021/acs.inorgchem.1c00113
Inorg. Chem. 2021, 60, 8500−8506

From these fits, the nearest-neighbor correlation is found to be ferromagnetic and all other significant magnetic correlations, which are between atoms separated by less than 10 Å, are antiferromagnetic as seen in the inset of Figure 7. A number of weak ferromagnetic correlations between atoms separated by 5−12 Å distances also exist, but these all appear to be associated with cations connected to each other through a sequence of nearest-neighbor distances and are therefore likely a result of the ferromagnetic nearest-neighbor correlations. Comparing the correlations in this paramagnetic phase with the ordered antiferromagnetic structure suggests that the nearest-neighbor ferromagnetic interaction competes, and ultimately loses out, to the second-nearest-neighbor antiferromagnetic coupling due to the higher degeneracy of the coupling through the cubic site.

Taken as a whole, the 120° antiferromagnetic ground state we have determined is fully consistent with prior studies on garnets with magnetism isolated to the tetrahedral sublattice.[27] Upon removing magnetic cations from the octahedral sublattice, the moments on the tetrahedral sites cant away from the (111) axis of the cubic structure and instead orient antiparallel across the shared edge of the cubic sites, much like what Geller and co-workers[16] proposed and what Dodokin et al. observed using Mössbauer spectroscopy.[15] Indeed, we even observe the short-range canting of the moments predicted through theoretical calculations by Rosencwaig[28] and Smirnov.[29] It is particularly interesting to recognize that our results suggest that the origin of the 120° orientation of the spins derives from antiferromagnetic coupling through the cubic site. These findings shed new light on the magnetic coupling between neighboring tetrahedra and how the cubic and octahedral sites mediate such interactions.

SUMMARY

The magnetic structures of $Ca_2YZr_2Fe_3O_{12}$ and $Ca_2LaZr_2Fe_3O_{12}$ have been determined using powder neutron diffraction and symmetry analysis, which reveals the coexistence of both long- and short-range magnetic order. Both compositions order in a noncollinear fashion at 18 and 21 K for $Ca_2YZr_2Fe_3O_{12}$ and $Ca_2LaZr_2Fe_3O_{12}$, respectively, with the minor change in the ordering temperatures attributed to the smaller tetrahedral sites in the Y versus the La phase. Most importantly, this work highlights the impact of the cubic site in mediating magnetic interactions between neighboring tetrahedral sites, which is frequently overlooked.

ASSOCIATED CONTENT

Supporting Information

The Supporting Information is available free of charge at https://pubs.acs.org/doi/10.1021/acs.inorgchem.1c00113.

Table S1, magnetization vector components; Tables S2 and S3, Rietveld refinement results of the powder neutron diffraction data for both materials; Figure S1, figures of Rietveld refinements; Figure S2, the specific heat of each respective material; Figure S3, isothermal $M-H$ measurements of each respective material; Figure S4, alternating current magnetic susceptibility at multiple frequencies; Figure S5, the diffuse scattering peaks in neutron powder diffraction at low two-θ; and Figure S6, illustrations of the respective magnetic structures (PDF)

AUTHOR INFORMATION

Corresponding Author

Brent C. Melot − *Department of Chemistry, University of Southern California, Los Angeles, California 90089, United States;* orcid.org/0000-0002-7078-8206; Email: melot@usc.edu

Authors

JoAnna Milam-Guerrero − *Department of Chemistry, University of Southern California, Los Angeles, California 90089, United States*

Michelle Zheng − *Department of Chemistry, University of Southern California, Los Angeles, California 90089, United States*

Nicole R. Spence − *Department of Chemistry, University of Southern California, Los Angeles, California 90089, United States*

Mario Falsaperna − *School of Physical Sciences, University of Kent, Canterbury CT2 7NH, United Kingdom*

Stuart Calder − *Neutron Scattering Division, Oak Ridge National Laboratory, Oak Ridge, Tennessee 37831, United States*

Saul Lapidus − *Advanced Photon Source, X-Ray Division, Argonne National Laboratory, Argonne, Illinois 60439, United States;* orcid.org/0000-0002-7486-4325

Paul J. Saines − *School of Physical Sciences, University of Kent, Canterbury CT2 7NH, United Kingdom;* orcid.org/0000-0002-4207-2112

Complete contact information is available at: https://pubs.acs.org/10.1021/acs.inorgchem.1c00113

Notes

The authors declare no competing financial interest.

ACKNOWLEDGMENTS

J.M.-G. and B.C.M. gratefully acknowledge support from the Office of Naval Research (Grant # N00014-15-1-2411). This research used resources at the High Flux Isotope Reactor, a DOE Office of Science User Facility operated by the Oak Ridge National Laboratory. Use of the Advanced Photon Source at Argonne National Laboratory was supported by the U.S. Department of Energy, Office of Science, Office of Basic Energy Sciences, under Contract No. DE-AC02-06CH11357. M.F. and P.J.S. would like to thank the Leverhulme Trust for funding via a research project grant (RPG-2018-268).

REFERENCES

(1) Bertaut, F.; Forrat, F. Structure des ferrites ferrimagnetiques de terres rares. *C. R. Hebd. Seances Acad. Sci.* **1956**, *242*, 382.

(2) Geller, S.; Gilleo, M. The crystal structure and ferrimagnetism of yttrium-iron garnet, $Y_3Fe_2(FeO_4)_3$. *J. Phys. Chem. Solids* **1957**, *3*, 30−36.

(3) Ustinov, A.; Tiberkevich, V.; Srinivasan, G.; Slavin, A.; Semenoc, A.; Karmanenko, S.; Kalinikos, B.; Mantese, J.; Ramer, R. Multiferroic magnetoelectric composites: Historical perspective, status, and future directions. *J. Appl. Phys.* **2006**, *100*, No. 093905.

(4) Mallmann, E.; Sombra, S.; Goes, J.; Fechine, P. Yttrium Iron Garnet: Properties and Applications Review. *Solid State Phenom.* **2013**, *202*, 65−96.

(5) Hahn, C.; de Loubens, G.; Klein, O.; Viret, M.; Naletov, V. V.; Ben Youssef, J. Comparative measurements of inverse spin Hall effects and magnetoresistance in YIG/Pt and YIG/Ta. *Phys. Rev. B* **2013**, *87*, No. 174417.

(6) Petrenko, O. A.; Ritter, C.; Yethiraj, M.; McK Paul, D. Investigation of the Low-Temperature Spin-Liquid Behavior of the Frustrated Magnet Gadolinium Gallium Garnet. *Phys. Rev. Lett.* **1998**, *80*, No. 4570.
(7) Florea, O.; Lhotel, E.; Jacobsen, H.; Knee, C. S.; Deen, P. P. Absence of magnetic ordering and field-induced phase diagram in the gadolinium aluminum garnet. *Phys. Rev. B* **2017**, *96*, No. 220413.
(8) Kinney, W. I.; Wolf, W. P. Magnetic interactions and short range order in gadolinium gallium garnet. *J. Appl. Phys.* **1979**, *50*, 2115−2117.
(9) Milam-Guerrero, J.; Neer, A. J.; Melot, B. C. Crystal chemistry and competing magnetic exchange interactions in oxide garnets and spinels. *J. Solid State Chem.* **2019**, *274*, 1−9.
(10) Prandl, W. Rhombohedral Magnetic Structure in Spessartite Type Garnets. *Phys. Status Solidi B* **1973**, *55*, K159−K163.
(11) Valyanskaya, T. V.; Plakhtii, V. P.; Sokolov, V. I. Antiferromagnetism of the garnet $Mn_3Al_2Ge_3O_{12}$. *Sov. Phys. − JETP* **1976**, *43*, 1189−1192.
(12) Lau, G. C.; Klimczuk, T.; Ronning, F.; McQueen, T. M.; Cava, R. J. Magnetic properties of the garnet and glass forms of $Mn_3Al_2Si_3O_{12}$. *Phys. Rev. B* **2009**, *80*, No. 214414.
(13) Neer, A. J.; Milam-Guerrero, J.; So, J. E.; Melot, B. C.; Ross, K. A.; Hulvey, Z.; Brown, C. M.; Sokol, A. A.; Scanlon, D. O. Ising-like antiferromagnetism on the octahedral sublattice of a cobalt-containing garnet and the potential for quantum criticality. *Phys. Rev. B* **2017**, *95*, No. 144419.
(14) Prandl, W. Magnetic Structure and Space Group of the Garnet $Ca_3Cr_2(GeO_4)_3$. *Solid State Commun.* **1972**, *11*, 645−647.
(15) Dodokin, A.; Lyubutin, I.; Mill, B.; Peshkov, V. Mossbauer Effect in Antiferromagnetic Substances with Garnet Structures. *Sov. Phys. − JETP* **1973**, *36*, 526−529.
(16) Geller, S.; Williams, H. J.; Espinosa, G. P.; Sherwood, R. C. Importance of Intrasublattice Magnetic Interactions and of Substitutional Ion Type in the Behavior of Substituted Yttrium Iron Garnets. *Bell Syst. Tech. J.* **1964**, *43*, 565−623.
(17) Tari, A. *The Specific Heat of Matter at Low Temperatures*; Imperial College Press, 2003.
(18) Paddison, J. A. M.; Ross Stewart, J.; Goodwin, A. L. spinvert: a program for refinement of paramagnetic diffuse scattering data. *J. Phys.: Condens. Matter* **2013**, *25*, No. 454220.
(19) Bogoslovskii, S. A.; Sokolov, V. Magnetic phase diagram of the garnet $Mn_3Cr_2Ge_3O_{12}$. *Sov. J. Exp. Theor. Phys. Lett.* **1982**, *35*, 61.
(20) Day, M.; Selbin, J. *Theoretical Inorganic Chemistry*, 2nd ed.; Reinhold Book Corporation: New York, 1962.
(21) Lahoubi, M. Group theory analysis of the rhombohedral magnetic structures in rare earth iron garnets revisited. *J. Phys.: Conf. Ser.* **2015**, *574*, No. 012099.
(22) Rodic, D.; Mitric, M.; Tellgren, R.; Rundlof, H.; Kremenovic, A. True magnetic structure of the ferrimagnetic garnet $Y_3Fe_5O_{12}$ and magnetic moments of iron ions. *J. Magn. Magn. Mater.* **1999**, *191*, 137−145.
(23) Princep, A. J.; Ewings, R. A.; Ward, S.; Toth, S.; Dubs, C.; Prabhakaran, D.; Boothroyd, A. T. The full magnon spectrum of yttrium iron garnet. *npj Quantum Mater.* **2017**, *2*, No. 63.
(24) Ivantchev, S.; Kroumova, E.; Madariaga, G.; Perez-Mato, J.; Aroyo, M. SUBGROUPGRAPH - a computer program for analysis of group-subgroup relations between space groups. *J. Appl. Crystallogr.* **2000**, *33*, 1190−1191.
(25) Aroyo, M. I.; Perez-Mato, J. M.; Orobengoa, D.; Tasci, E.; de la Flor, G.; Kirov, A. Crystallography online: Bilbao Crystallographic Server. *Bulg. Chem. Commun.* **2011**, *43*, 183−197.
(26) Wills, A. S. A new protocol for the determination of magnetic structures using simulated annealing and representational analysis (SARA*h*). *Phys. B: Condens. Matter* **2000**, *276*−*278*, 680.
(27) Plakhtii, V. P.; Golosovskii, I. V.; Bedrisova, M. N.; Smirnov, O. P.; Sokolov, V. I.; Mill, B. V.; Parfenova, N. N. Magnetic ordering and bond geometry in garnets with Fe3+ ions in the tetrahedral sublattice. *Phys. Status Solidi A* **1977**, *39*, 683−695.
(28) Rosencwaig, A. Localized canting model for substituted ferrimagnets. I. Singly substituted YIG systems. *Can. J. Phys.* **1970**, *48*, 2857−2867.
(29) Smirnov, O. P.; Plakhty, V. P. On the Role of Intrasublattice Interactions in YIG with Diamagnetically Substituted a-Sublattice. *Phys. Status Solidi A* **1983**, *77*, 505−511.

https://doi.org/10.1021/acs.inorgchem.1c00113
Inorg. Chem. 2021, 60, 8500−8506